Supplementary Information (SI) for Journal of Materials Chemistry C.

Supplementary Material

Theoretical Giant Circular Dichroism and Broadband Asymmetric Absorption Enabled by Multilayered Chiral Metastructures-Photonic Crystals in the Near-Infrared Regime

Shu-Hui Zhu[1], Hai-Feng Zhang[1]*
[1]College of Electronic and Optical Engineering and the College of Flexible Electronics (Future Technology), Nanjing University of Posts and Telecommunications, Nanjing, 210023, China.
*e-mail: hanlor@njupt.edu.cn or hanlor@163.com)

1. The fabrication of the proposed MCMPC

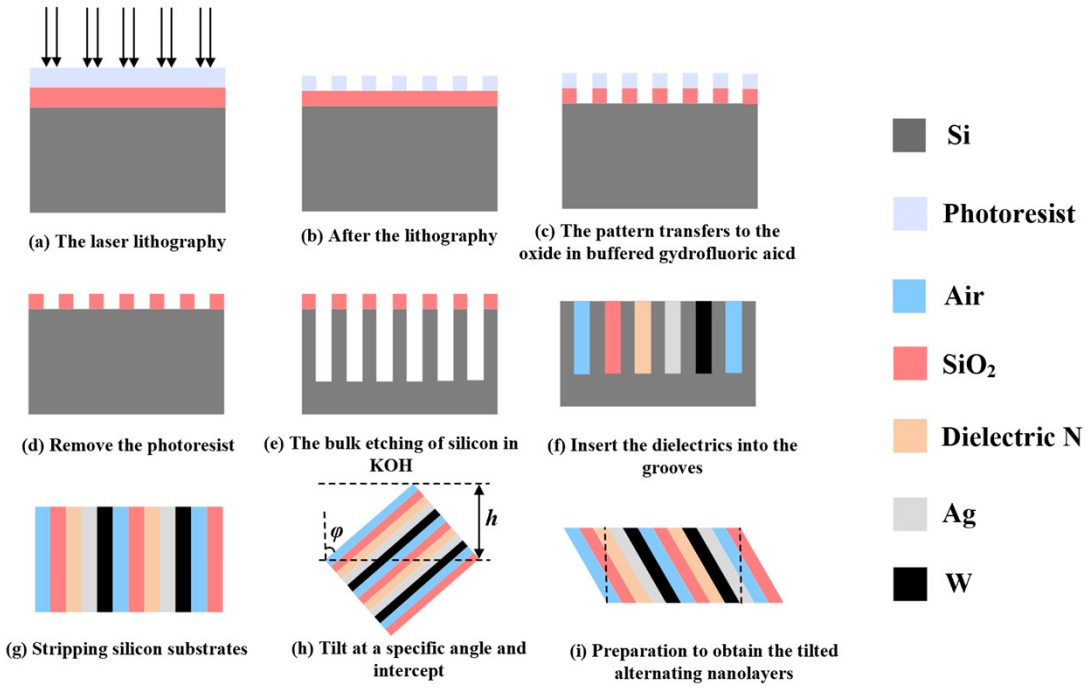

Fig. S1. The diagrams of the fabrication process flow of the proposed MPC. The specific materials are denoted expressly on the right side of the process flow.

The hierarchical configuration proposed in this study is a theoretical design primarily aimed at achieving optimal theoretical performance, with less emphasis on fabrication feasibility. However, if practical fabrication is required, it can be implemented as follows:

1. Substrate Preparation and Etching Process

In the manufacturing process, etching techniques are employed [1]. A silicon wafer is selected as the substrate, and wet anisotropic etching is utilized to fabricate annular grooves of varying depths on the silicon wafer. These grooves correspond to the different constituent materials and their respective scales in the proposed metastructures-photonic crystals (MPC). Specifically, the wet anisotropic etching is performed using a 44 wt%

aqueous potassium hydroxide (KOH) solution at 85 °C, with a thermally grown SiO_2 layer serving as a hard mask during the etching process.

2. Material Deposition and Structural Formation

   Once the grooves matching the design specifications derived from our theoretical study are formed on the silicon substrate, metallic and dielectric materials are subsequently deposited into their designated positions. By stacking the aforementioned materials with the specified thicknesses as described in this work, an experimental realization of the MPC configuration can be achieved.

3. Theoretical Interpretation of the Fabricated Structure

   From a theoretical standpoint, when the height of the substrate is allowed to extend freely, the resulting structure can be regarded as an ideal metastructures-photonic crystal (MCMPC). Under these conditions, the absorption characteristics of the fabricated configuration align well with our theoretical predictions. The detailed fabrication procedure for the proposed structure is illustrated in Figs. S1(a)–(i).

2. The experimental setup for the designed MCMPC

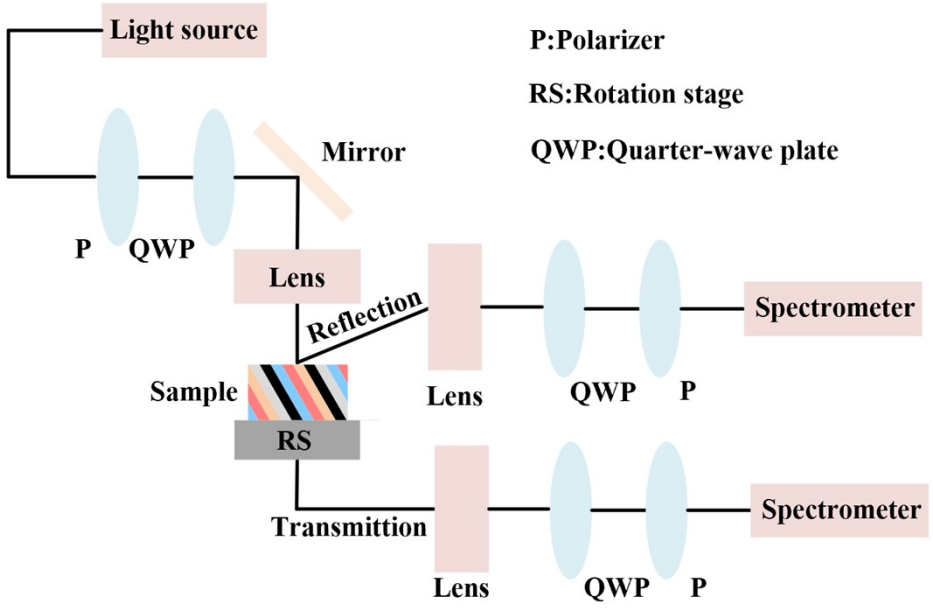

Fig. S2. The experiment setup of the detection function of the MCMPC.

As shown in Fig. S2, the experimental setup for proposed MCMPC is summarized as follows [2].

1. Optical Setup and Circular Polarization Generation

   Circularly polarized waves are generated by directing the laser beam through a broadband linear polarizer and then a quarter-wave plate.

2. Sample Illumination and Angular Measurements

   The incident wave is focused onto the sample with a 5 cm focal length lens. The sample is mounted on a rotation stage to enable angular-dependent transmission and reflection measurements.

3. Signal Collection and Polarization Analysis

   Transmitted and reflected signals are collected with a spectrophotometer to study absorption. A circular polarizer comprising a quarter-wave plate and a linear polarizer was placed before the spectrometer for polarization state analysis.

3. Theoretical Modeling and Derivation for the MCMPC

The Maxwell-Garnett homogenized effective relative permittivity tensor of MPC1 is expressed in the *x'y'z'* coordinate frame[2]:

$$\overline{\varepsilon}' = \begin{bmatrix} \varepsilon'_{xx} & 0 & 0 \\ 0 & \varepsilon'_{yy} & 0 \\ 0 & 0 & \varepsilon'_{zz} \end{bmatrix} \tag{S1}$$

where $\varepsilon'_{xx} = \dfrac{\sum_{j=A}^{K} d_j}{\sum_{j=A}^{K} d_j / \varepsilon_{j_{(Mat)}}}$, and $\varepsilon'_{yy} = \varepsilon'_{zz} = \dfrac{\sum_{j=A}^{K} d_j \varepsilon_{j_{(Mat)}}}{\sum_{j=A}^{K} d_j}$ is the dielectric constant of the unit layer material corresponding to *j*.

In the *x'y'z'* coordinate system, the electric displacement vector ***D'*** and electric field vector ***E'*** satisfy the following relation [2]:

$$\boldsymbol{D}' = \varepsilon_0 \overline{\varepsilon}' \boldsymbol{E}' \tag{S2}$$

Furthermore, there exists a transformation relationship between the *xyz* and *x'y'z'* coordinate systems, given by [2]:

$$\begin{bmatrix} x \\ y \\ z \end{bmatrix} = \begin{bmatrix} \cos\varphi_1 & 0 & \sin\varphi_1 \\ 0 & 1 & 0 \\ -\sin\varphi_1 & 0 & \cos\varphi_1 \end{bmatrix} \begin{bmatrix} x' \\ y' \\ z' \end{bmatrix} \tag{S3}$$

Within the *xyz* reference system, ***D*** and ***E*** are characterized by the following relationship [2]:

$$\boldsymbol{D} = \varepsilon_0 \overline{\varepsilon} \boldsymbol{E} \tag{S4}$$

The effective relative permittivity tensor of MPC1 is transformed in the *xyz* coordinate system as follows [2]：

$$\varepsilon = \begin{bmatrix} \varepsilon_{xx} & 0 & \varepsilon_{xz} \\ 0 & \varepsilon_{yy} & 0 \\ \varepsilon_{zx} & 0 & \varepsilon_{zz} \end{bmatrix} \tag{S5}$$

where ε_{xx}, ε_{yy}, ε_{zz}, ε_{xz}, and ε_{zx} can be represented as [2]

$$\begin{aligned} \varepsilon_{xx} &= \varepsilon'_{xx} \cos^2\varphi_1 + \varepsilon'_{yy} \sin^2\varphi_1 \\ \varepsilon_{yy} &= \varepsilon'_{yy} \\ \varepsilon_{zz} &= \varepsilon'_{xx} \sin^2\varphi_1 + \varepsilon'_{yy} \cos^2\varphi_1 \\ \varepsilon_{xz} &= \varepsilon_{zx} = (\varepsilon'_{yy} - \varepsilon'_{xx}) \sin\varphi_1 \cos\varphi_1 \end{aligned} \tag{S6}$$

The magnetic field of the RCP wave follows from the source-free Maxwell equations:

$$\boldsymbol{H} = H_0[e^{j(kz-\omega t)}\vec{x} - je^{j(kz-\omega t)}\vec{y}] \tag{S7}$$

When the CPWs excite MPC1, the wave vectors of the forward (+*z*-direction) and backward (-*z*-direction) propagating waves exhibit significant disparities due to the combined effects of a tilted optical axis and nonzero incidence angle at the boundary. From Eq. S8, it can be inferred that for both the forward and backward incidence of RCP waves, the magnetic field can be expressed as [2]:

$$\boldsymbol{H} = [H_x^+ e^{j(k_z^+ z + k_x x - \omega t)} + H_x^- e^{j(k_z^- z + k_x x - \omega t)}]\vec{x} - j[H_y^+ e^{j(k_z^+ z + k_x x - \omega t)} + H_y^- e^{j(k_z^- z + k_x x - \omega t)}]\vec{y} \tag{S8}$$

where k_z^+ and k_z^- indicate the +*z* and -*z* components of the wave vectors, respectively. Thus, we have [2]

$$\nabla \times \boldsymbol{H} = \begin{pmatrix} \vec{x} & \vec{y} & \vec{z} \\ \dfrac{\partial}{\partial x} & \dfrac{\partial}{\partial y} & \dfrac{\partial}{\partial z} \\ H_x & H_y & 0 \end{pmatrix} = (-H_y^+ k_z^+ - H_y^- k_z^-)\vec{x} + (jH_x^+ k_z^+ + jH_x^- k_z^-)\vec{y} + k_x(H_y^+ + H_y^-)\vec{z} \tag{S9}$$

Based on Eqs. S5 and S6, it follows that [2]

$$\begin{pmatrix} D_x \\ D_y \\ D_z \end{pmatrix} = \varepsilon_0 \begin{pmatrix} \varepsilon_{xx} & 0 & \varepsilon_{xz} \\ 0 & \varepsilon_{yy} & 0 \\ \varepsilon_{zx} & 0 & \varepsilon_{zz} \end{pmatrix} \begin{pmatrix} E_x \\ E_y \\ E_z \end{pmatrix} \tag{S10}$$

$$\frac{\partial \boldsymbol{D}}{\partial t} = -j\omega\varepsilon_0(\varepsilon_{xx}E_x + \varepsilon_{xz}E_z)\hat{x} + \omega\varepsilon_0\varepsilon_{yy}E_y\hat{y} - j\omega\varepsilon_0(\varepsilon_{zx}E_x + \varepsilon_{zz}E_z)\hat{z} \tag{S11}$$

From $\nabla \times \boldsymbol{H} = \frac{\partial \boldsymbol{D}}{\partial t}$, the following equations are derived [2]:

$$\begin{cases} H_y^+ k_z^+ + H_y^- k_z^- = j\omega\varepsilon_0(\varepsilon_{xx}E_x + \varepsilon_{xz}E_z) \\ j(H_x^+ k_z^+ + H_x^- k_z^-) = \omega\varepsilon_0\varepsilon_{yy}E_y \\ k_x(H_y^+ + H_y^-) = -j\omega\varepsilon_0(\varepsilon_{zx}E_x + \varepsilon_{zz}E_z) \end{cases} \tag{S12}$$

Then, E_x, E_y, and E_z are derived from Eq. S13, and the result is [2]

$$\begin{cases} E_x = \dfrac{\varepsilon_{zz}k_z^+ + \varepsilon_{xz}k_x}{j\omega\varepsilon_0(\varepsilon_{xx}\varepsilon_{zz} - \varepsilon_{xz}^2)} H_y^+ + \dfrac{\varepsilon_{zz}k_z^- + \varepsilon_{xz}k_x}{j\omega\varepsilon_0(\varepsilon_{xx}\varepsilon_{zz} - \varepsilon_{xz}^2)} H_y^- \\ E_y = \dfrac{jk_z^+}{\omega\varepsilon_0\varepsilon_{yy}} H_x^+ + \dfrac{jk_z^-}{\omega\varepsilon_0\varepsilon_{yy}} H_x^- \\ E_z = -\dfrac{\varepsilon_{zx}k_z^+ + \varepsilon_{xx}k_x}{j\omega\varepsilon_0(\varepsilon_{xx}\varepsilon_{zz} - \varepsilon_{xz}^2)} H_y^+ - \dfrac{\varepsilon_{zx}k_z^- + \varepsilon_{xx}k_x}{j\omega\varepsilon_0(\varepsilon_{xx}\varepsilon_{zz} - \varepsilon_{xz}^2)} H_y^- \end{cases} \tag{S13}$$

For the +*z*-direction RCP wave, from $\nabla \times \boldsymbol{E} = -\frac{\partial \boldsymbol{B}}{\partial t}$, we can obtain [2]

$$\begin{cases} \dfrac{\partial E_x}{\partial z} - \dfrac{\partial E_z}{\partial x} = \omega\mu_0\mu H_y^+ \\ -\dfrac{\partial E_y}{\partial z} = j\omega\mu_0\mu H_x^+ \end{cases} \tag{S14}$$

By decomposing the RCP wave into TM and TE modes, the result is [2]

$$\begin{cases} \varepsilon_{zz}k_{z(\mathrm{TM})}^2 + (\varepsilon_{xz}k_x + \varepsilon_{zx}k_x)k_{z(\mathrm{TM})} + \varepsilon_{xx}k_x^2 = k_0^2(\varepsilon_{xx}\varepsilon_{zz} - \varepsilon_{xz}^2) \\ k_{z(\mathrm{TE})} = k_0{}^2 j\varepsilon_{yy} \end{cases} \tag{S15}$$

From Eq. S16, we can obtain solutions for $k_{z(TM)}$ and $k_{z(TE)}$, respectively, which are as follows [2]

$$\begin{cases} k_{z(\mathrm{TM})} = \dfrac{-\varepsilon_{xz}k_x \pm \sqrt{(\varepsilon_{xz}^2 - \varepsilon_{zz}\varepsilon_{xx})(k_x^2 - k_0^2\varepsilon_{zz})}}{\varepsilon_{zz}} \\ k_{z(\mathrm{TE})} = \pm k_0\sqrt{j\varepsilon_{yy}} \end{cases} \tag{S16}$$

$$\frac{\partial \boldsymbol{D}}{\partial t} = -j\omega\varepsilon_0(\varepsilon_{xx}E_x + \varepsilon_{xz}E_z)\hat{x} + \omega\varepsilon_0\varepsilon_{yy}E_y\hat{y} - j\omega\varepsilon_0(\varepsilon_{zx}E_x + \varepsilon_{zz}E_z)\hat{z} \tag{S17}$$

Consequently, the following results can be further deduced [2]:

$$k_z^1 = \frac{-\varepsilon_{xz}k_x + \sqrt{(\varepsilon_{xz}^2 - \varepsilon_{zz}\varepsilon_{xx})(k_x^2 - k_0^2\varepsilon_{zz})}}{\varepsilon_{zz}} + k_0\sqrt{j\varepsilon_{yy}} \tag{S18}$$

$$k_z^2 = \frac{-\varepsilon_{xz}k_x - \sqrt{(\varepsilon_{xz}^2 - \varepsilon_{zz}\varepsilon_{xx})(k_x^2 - k_0^2\varepsilon_{zz})}}{\varepsilon_{zz}} - k_0\sqrt{j\varepsilon_{yy}} \tag{S19}$$

where $k_x = k_0 \sin\theta$, and $k_0 = \omega / c$. Moreover, k_z represents the normal component of the wave vector for the RCP wave. The two distinct solutions, k_z^1 and k_z^2, suggest that the RCP wave can propagate in two opposite directions.

Regarding the assumption of isotropic inclusions, while the classical theory is indeed based on this premise, our work extends its applicability by employing a coordinate transformation (Eq. (S3)) to macroscopically equate the tilted metal layers into an effective anisotropic medium. Concerning the condition of low volume fraction, we performed a quantitative assessment using the MPC1 unit as an example. The total thickness of the metal layers is 381.5 nm, while the period of a full unit is 1862.5 nm, resulting in a metal filling fraction of approximately 20.5%,

which satisfies the low volume fraction criterion. Pertaining to the quasi-static limit, the operational wavelengths in our near-infrared regime (0.789–1.071 μm) are substantially larger than the characteristic dimensions of the unit layers. Under this condition, the effective permittivity tensor is predominantly determined by the material parameters and geometric configuration, independent of the incident wave frequency, thus fulfilling the prerequisite for the quasi-static approximation. In summary, we contend that the application of the Maxwell-Garnett approximation is reasonable and valid for the analysis of the MCMPC.

4. The normalized surface impedance for forward RCP and LCP waves in MPC1

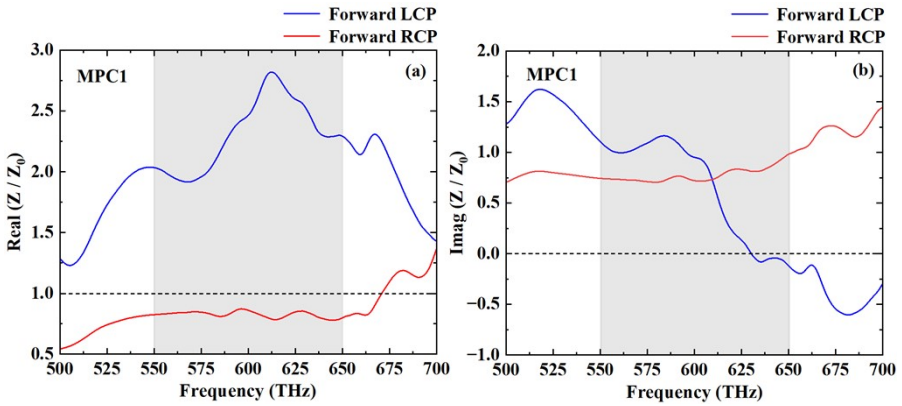

Fig. S3. (a) Real and (b) imaginary parts of the normalized surface impedance for forward-propagating RCP and LCP waves in MPC1.

As shown in Figs. S3(a) and (b), within 550~650 THz, the real part of the normalized surface impedance $\frac{Z_{RCP}}{Z_0}$ for the forward-propagating RCP wave approaches 0, whereas the imaginary part remains minimal, demonstrating excellent impedance matching and highly efficient absorption within this spectral band. In contrast, the normalized impedance real part of $\frac{Z_{LCP}}{Z_0}$ for the LCP wave significantly deviates from 1, which is indicative of strong surface reflection.

5. Simulation setup for the MCMPC

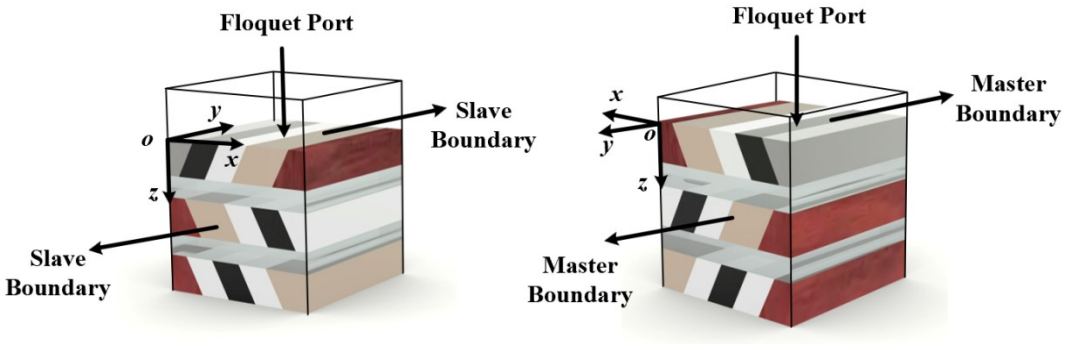

Fig. S4. Simulated port and boundary Settings in HFSS.

In Fig.S4, the three-dimensional numerical analysis of the proposed MCMPC was conducted using the commercial finite element method (FEM) solver, ANSYS High-Frequency Structure Simulator (HFSS). The key

configuration settings are as follows:

1. Numerical Solver: The simulations were performed using the Finite Element Method (FEM) within the HFSS environment to accurately resolve the electromagnetic field distributions.
2. Periodic Boundary Conditions: Master/Slave boundary conditions were applied along the *x* and *y* directions of the unit cell to emulate the response of an infinite, periodic array.
3. Excitation and Analysis: Floquet ports were employed as the excitation and analysis interfaces for the periodic structure. These ports were positioned directly above and below the unit cell to simulate plane wave incidence and to calculate the reflection and transmission coefficients.
4. Wave Excitation and Polarization Analysis: The structure was illuminated with normally incident left-handed circularly polarized (LCP) and right-handed circularly polarized (RCP) waves, propagating along the +*z*-axis. This setup enabled the characterization of the polarization-dependent response.

6. Errors analysis for the MCMPC

Fig. S5(a) shows the exceptional modulation effects of the polarization angle α on the CD characteristics of the MCMPC. The measured CD exhibits a nonmonotonic angular dependence, initially increasing and then decreasing with varying α. At α = -24°, the CD reaches its maximum value of 0.77 at 328 THz. However, when α = -52°, the CD resonance peak shifts to 369 THz with a reduced value of 0.6. In Fig. S5(b) , the AAC reaches a distinct peak value of 0.78 at 327 THz for α = -24°. As α changes to -52°, the AAC response shifts to 372 THz, decreasing to 0.67 relative to its original peak value. Fig. S5(c) presents the angular-dependent variations in absorption under forward RCP wave, where the peak absorption frequency exhibits a significantly blueshifts (from 326 to 374 THz) with increasing absolute values of α. The maximum absorption of 0.95 occurs at 326 THz for α = -24°, corresponding to an *OB* of 315~364 THz with an *RB* of 14.4%. When α decreases to -10°, the absorption peak decreases to 0.91 at 334 THz, accompanied by a narrowed *OB* of 324~350 THz. A further increase in α to -38°and -52°shifts the peak absorption frequencies to 372 THz and 374 THz, respectively. This dual modulation mechanism enables coordinated control over both intensity and wavelength-specific responses. To address the practical challenges and potential experimental errors associated with polarization control, our analysis demonstrates that the device performance remains robust within a certain range of angular deviations. As shown in Fig. S5, even with a ±10° deviation from the optimal polarization angle, the CD value exceeds 0.7 and the forward RCP absorption remains above 0.9 across a broad bandwidth. This indicates that the proposed configuration can tolerate realistic misalignments in polarization without significant degradation of its core functional performance.

As shown in Fig. S6(a), when h_1 is 80 nm, the maximum CD value of 0.78 occurs at 332 THz. As h_1 increases to 110 nm, the peak of CD shifts to lower frequencies at 310 THz but decreases to 0.69. In Fig. S6(b), the AAC reaches 0.79 at 327 THz when h_1 = 80 nm. When h_1 is increased to 110 nm, the peak of the AAC shifts to 317 THz, with a reduced value of 0.73. Fig. S6(c) shows the absorption spectrum dependence on h_1. A strong absorption peak of 0.96 is achieved at 332 THz for h_1 = 80 nm, with an *OB* spanning 312 to 367 THz and an *RB* of 16.2% for the absorption exceeding 0.9. However, when h_1 is increased to 90 nm, the peak of absorption shifts to 320 THz, and the *OB* narrows to the range of 311 to 355 THz, with an *RB* of 13.2%. Upon further increasing h_1 to 100 nm, the peak shifts to 318 THz, and the *OB* is further reduced to 318~341 THz with an *RB* of 7%. From Fig. S6(d), the highest CD of 0.78 is observed at 336 THz for h_3 = 110 nm, but when h_3 increases to 140 nm, the peak shifts to 325 THz, accompanied by a decrease to 0.76. At h_3 = 155 nm, the peak is further redshifts to 356 THz, and the CD value decreases to 0.74. In Fig. S6(e), the maximum AAC of 0.8 is obtained at 334 THz for h_3 = 110 nm. However, at h_3 = 140 nm, the peak shifts to 326 THz and decreases to 0.76, whereas at h_3 = 155 nm, it further shifts to 340 THz, and the peak of the AAC decreases to 0.74. Considering potential fabrication tolerances in layer thickness, our

parameter sweep provides a direct assessment of the associated performance deviations. For h_1, a fabrication error of ±10 nm leads to a controllable spectral shift, with the absorption peak remaining above 0.85. Similarly, for h_3, a ±10 nm deviation primarily induces a shift in the peak frequencies of CD and AAC, while the corresponding peak magnitudes exhibit only limited degradation,demonstrating that the structure is equally robust against fabrication errors in h_3.

A systematic investigation of the impact of φ_i variations in MPC units on MCMPC performance metrics is presented in Figs. S7. As shown in Fig. S7(a), the peak of CD gradually decreases from 0.79 at 330 THz to 0.74 at 334 THz as φ_1 increases from 51.6° to 52.2°. In Fig. S7(b), the peak AAC decreases from 0.79 at 332 THz to 0.76 at 357 THz as φ_1 increases from 51.6° to 52.2°. Fig. S7(c) shows that at φ_1 = 51.6° and 51.8°, the *OB*s with absorption exceeding 0.9 span 312~367 THz and 315~359 THz, corresponding to *RB*s of 16.2% and 13%, respectively. The observed reduction in CD and AAC with increasing φ_1 is attributed to the diminished plasmon coupling between adjacent MPC units. In Fig. S7(d), the CD achieves a peak value of 0.74 at 329 THz for φ_2 = 51.2°, which increases to 0.78 at 332 THz when φ_2 = 51.6° and subsequently decreases to 0.77 at 323 THz for φ_2 = 51.8°. Fig. S7(e) displays that the AAC reaches a maximum of 0.77 at 355 THz under φ_2 = 51.2°, increases to 0.79 at 327 THz for φ_2 = 51.6°, and finally decreases to 0.77 at 324 THz when φ_2= 51.8°. These findings collectively demonstrate that the geometric parameters of MPC1 are critical structural variables that play a dominant role in governing the CD and AAC performance of MCMPC. This layer-specific parameter sensitivity highlights the importance of precise control of MPC1 for optimizing the functionality of chiral MPCs . A small angular error of ±0.2° for φ_1 and φ_2 around their respective optima results in a very modest decrease in the peak CD (by <0.03) and AAC (by <0.02). Critically, the operating bandwidth for high *OB* remains largely unaffected within this error margin.

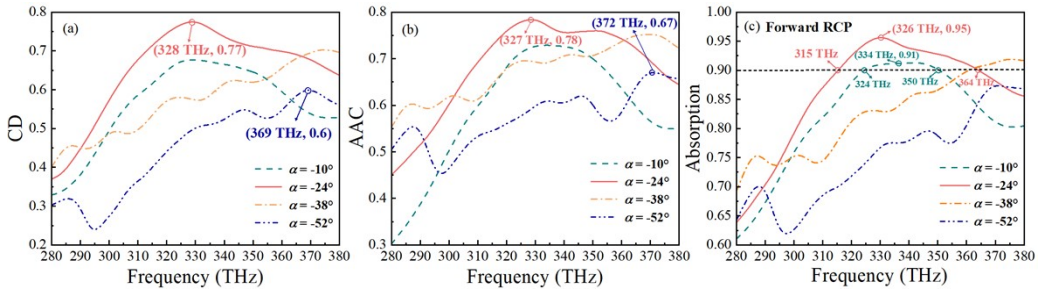

Fig. S5. Influences of the variation in the polarization angle α on the (a) CD curves, (b) AAC curves, and (c) absorption of the forward RCP wave for the MCMCP.

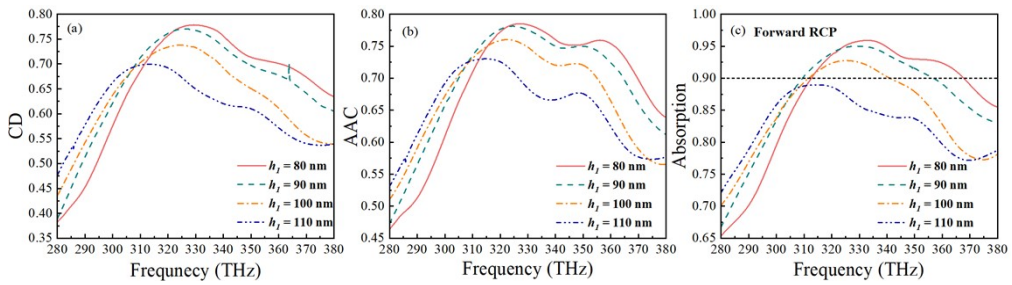

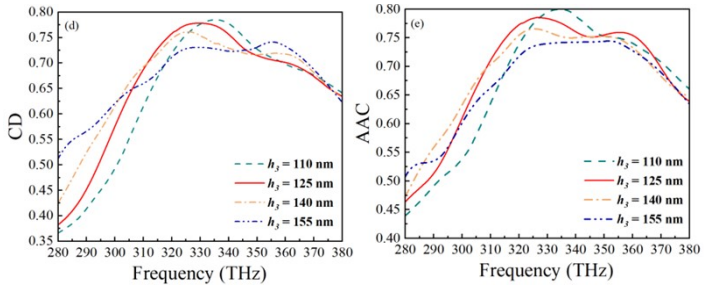

Fig. S6. Impact of the vertical heights of MPC1 and MPC2 on the performance of MCMPC. Effects of h_1 on (a) CD, (b) AAC and (c) absorption under the incident of forward RCP waves. Effects of h_3 on (d) CD and (e) AAC.

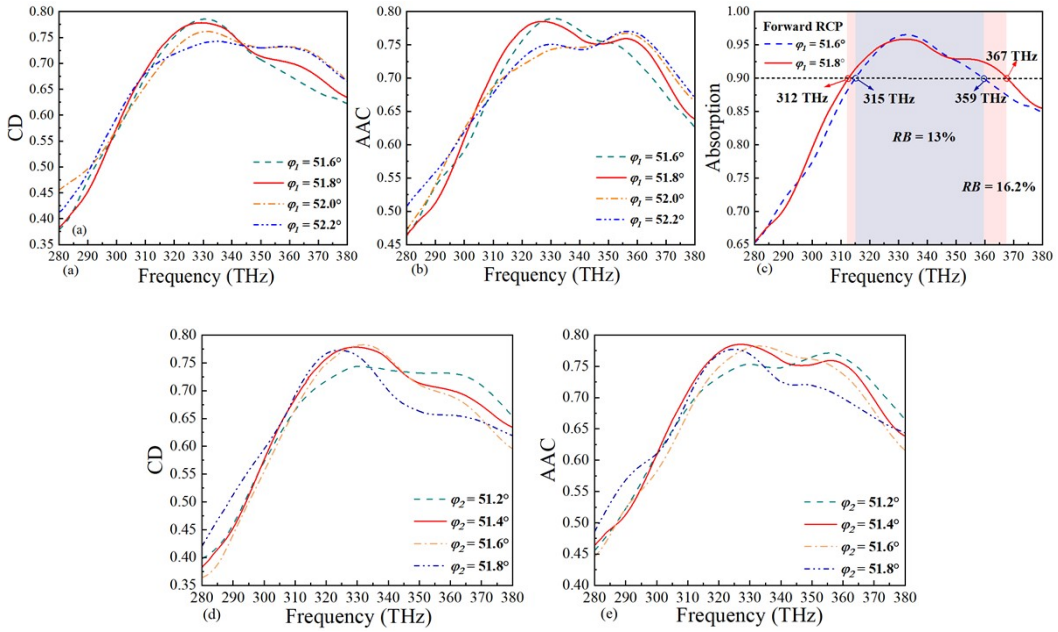

Fig. S7. The impact of the tilt angles for the MPC1 and MPC2 on the performance of MCMPC. Effects of φ_1 on the (a) CD, (b) AAC and (c) absorption bandwidths under forward RCP waves. Effects of φ_2 on (d) CD and (e) AAC.

References

1. B. K. Teo, X. H. Sun, Chemical Reviews, 2007, 107, 1454–1532.

2. T. Jia, et al., Opto-Electronic Advances, 2025.

3. Y. T. Fang and Y. C. Zhang, Plasmonics, 2018, 13, 661-667.